

Amplification of turbulence in contracting prestellar cores in primordial minihalos

SHO HIGASHI ¹, HAJIME SUSU ¹ AND GEN CHIAKI ²

¹*Department of Physics, Konan University, Okamoto, Kobe, Japan*

²*Center for Relativistic Astrophysics, School of Physics, Georgia Institute of Technology, Atlanta, GA, USA*

(Received ???; Revised ???; Accepted ???)

Submitted to ApJ

ABSTRACT

We investigate the amplification of turbulence through gravitational contraction of the primordial gas in minihalos. We perform numerical simulations to follow the cloud collapse, assuming polytropic equations of state for different initial turbulent Mach numbers and resolutions. We find that the turbulent velocity is amplified solely by gravitational contraction, and eventually becomes comparable to the sound speed, even for small initial turbulent Mach numbers ($\mathcal{M}_0 \gtrsim 0.05$). We derive an analytic formula for the amplification of turbulent velocity in a collapsing cloud, and find that our numerical results are consistent with the formula. These results suggest that the turbulence can play an important role in collapsing clouds for general cases.

Keywords: stars: Population III — early Universe — turbulence — hydrodynamics — ISM: clouds — ISM: kinematics and dynamics

1. INTRODUCTION

Cosmological simulations based on the Λ CDM model predict that minihalos with $M \sim 10^6 M_\odot$ host the first generation of stars in the universe at redshifts $z \gtrsim 10$ (Haiman et al. 1996; Tegmark et al. 1997; Nishi & Susa 1999; Fuller & Couchman 2000; Abel et al. 2002; Bromm et al. 2002; Yoshida et al. 2003). It has been believed that the first stars are largely massive ($\sim 10\text{--}1000 M_\odot$) due to inefficient cooling in the primordial gas clouds (Omukai & Nishi 1998; Yoshida et al. 2008). However, recent numerical studies have revealed that the fragmentation of accretion disks can lead less massive stars ($\sim 1 M_\odot$) to form (Clark et al. 2011b; Greif et al. 2011, 2012; Susa 2013; Susa et al. 2014; Stacy et al. 2016; Hirano & Bromm 2017; Susa 2019; Inoue & Yoshida 2020; Chiaki & Yoshida 2020). In addition, turbulence can either promote (Clark et al. 2011a; Riaz et al. 2018; Wollenberg et al. 2020), or suppresses fragmentation due to the amplification of magnetic fields (Sur et al. 2010, 2012; Federrath et al. 2011; Turk et al. 2012; Machida & Doi 2013; Sharda et al. 2020).

Previous studies have shown that the turbulent velocity in minihalos has a similar scaling law to local Galactic molecular clouds (Larson 1981; Prieto et al. 2011). Greif et al. (2012) demonstrated that the tur-

bulent velocity is amplified during collapse and exceeds the sound speed at the end of the collapse phase. Turk et al. (2012) also showed that the vorticity of the gas is amplified during the collapse phase. In addition, they showed that sufficiently high-resolution simulations are required to accurately resolve the morphology of clouds deformed by the turbulence in minihalos. However, the driving mechanisms of turbulence have not been well studied.

The results of several cosmological simulations indicate that the accretion flow of gas along the filaments into halos can drive turbulence when dark matter and gas are virialized in minihalos (e.g., Wise & Abel 2007; Greif et al. 2008; Klessen & Hennebelle 2010). However, this amplification occurs in low density regions ($n_{\text{H}} \sim 10^3 \text{ cm}^{-3}$). The free-fall time of collapsing dense cores is much shorter, $\lesssim 4.7(n_{\text{H}}/10^8 \text{ cm}^{-3})^{-1/2}$ kyr, than the dynamical time of the mass accretion onto halos, $\sim 1.5(n_{\text{H}}/10^3 \text{ cm}^{-3})^{-1/2}$ Myr, i.e., the free-fall time scale with averaged density of the gas cloud in the minihalo. Hence, the accretion-driven turbulence may have negligible effects on the dense cores. Thus, the turbulence should be amplified by another driving source than the anisotropic gas accretion flow.

Robertson & Goldreich (2012), Birnboim et al. (2018), and Mandal et al. (2020) showed that the turbulent velocity could be amplified by the contraction of isothermal gas clouds. This can be explained in the analogy of the *inversely* expanding (i.e., contracting) uni-

verse. In contrast to the cosmological perturbation theory, where the amplitude of velocity fluctuations decays as the universe expands, it should be amplified in collapsing clouds. This mechanism is often quoted as ‘‘adiabatic heating’’ of turbulence.

Applying this argument to the central region of clouds hosted by minihalos, we expect that turbulence is amplified by gravitational contraction even with a very weak seed of turbulence at the onset of collapse. So far, any literature has not shown the detailed comparison of the adiabatic heating theory with numerical simulations of first star formation. In order to pin down the physical reason of the growth of turbulence in the first star forming core, we need to compare the results of numerical simulations with the theory, including the growth rate, the temporal evolution of the power spectrum, the fraction of the solenoidal modes, etc.

In this paper, we investigate the amplification of turbulence due to gravitational collapse by following gas contraction in minihalos until the end of the collapse phase. The numerical results are analyzed to be compared with the adiabatic heating theory. This paper is structured as follows. First, we analytically estimate a formula for the amplification of turbulence in Section 2. In Section 3, we describe the setup of numerical simulations. In Section 4, we present our results and compare them with our analytic model obtained in Section 2, and Section 5 is devoted for discussion. The main points in this paper are summarized in Section 6.

2. ANALYTIC ESTIMATE

In this section, we analytically evaluate the amplification of turbulence through gravitational contraction. Gas clouds in minihalos collapse in a self-similar fashion as well as molecular cloud cores in the present-day Universe. Those clouds have a core of Jeans length which contracts approximately uniformly, leaving the outer envelope with $\propto r^{-2.2}$ density distribution (e.g., Omukai & Nishi 1998; Yoshida et al. 2006). Here we focus our discussion on the growth of turbulence in this run-away collapsing core.

We consider the evolution of density/velocity fluctuations in an uniformly changing background. With the linear approximation, we obtain growth equations for the fluctuations of density $\delta \equiv \delta\rho/\rho$ and gravitational potential $\delta\phi$ as

$$\dot{\delta} + \nabla \cdot \mathbf{u} = 0, \quad (1)$$

$$\dot{\mathbf{u}} + 2H\mathbf{u} + a^{-2}\nabla\delta\phi + \frac{\nabla c_s^2\delta}{a^2} = 0, \quad (2)$$

$$a^2\nabla^2\delta\phi = 4\pi G\rho\delta. \quad (3)$$

from the equation of motion, the equation of continuity and the Poisson equation. In these equations, a and $H(= \dot{a}/a)$ denote the scale factor and the ‘‘Hubble parameter’’, respectively, that define the change of background density as $\rho \propto a^{-3}$. c_s denotes the sound speed,

∇ and \mathbf{u} are the gradient and peculiar velocity in the comoving frame, respectively. Taking the rotation of Equation (2), we obtain

$$\nabla \times \dot{\mathbf{u}} = -2H\nabla \times \mathbf{u}. \quad (4)$$

Integration of Equation (4) on both sides yields the scaling relation of the vorticity $\boldsymbol{\omega} \equiv \nabla \times \mathbf{u}$ as

$$\boldsymbol{\omega} \propto a^{-2} \propto \rho^{2/3}. \quad (5)$$

This indicates that amplitude of vorticity is proportional to the two-thirds power of the background density. Hence, the solenoidal mode of turbulence should grow monotonically in the collapsing background.

The relation (Equation 5) is valid even in the case that the velocity field is nonlinear. This can be explained by the fact that the vorticity equation is analogous to the induction equation of magnetic fields,

$$\frac{\partial \boldsymbol{\omega}}{\partial t} = \nabla \times (\mathbf{v} \times \boldsymbol{\omega}),$$

where the baroclinic term and the dissipation term are neglected. In ideal MHD, it is known that when the magnetic field is frozen with the fluid, the magnetic field increases with contraction by the power of two-thirds of the density, due to the conservation of magnetic flux. We can apply the same argument when magnetic field B is replaced with vorticity $\boldsymbol{\omega}$ from the similarity of their growth equations. In other words, $\boldsymbol{\omega}$ increases due to the conservation of circulation Γ :

$$\Gamma \equiv \oint \boldsymbol{\omega} \cdot d\mathbf{S}.$$

Note that we do not include the viscosity term in the vorticity equation which should play a role when shocks form and the turbulence saturates. Thus, Equation (5) is not valid in the saturated regime. In the numerical simulations of the present paper (Section 3), the viscosity term is also not included explicitly, since the viscous scale is too small to be resolved. However effective numerical viscosity always comes into play, which realizes the shock formation and the saturation of the turbulence in the simulations.

Similar to the argument on vorticity, we can discuss the divergence of the velocity field, which represents the compression mode of the turbulent flow. Taking the divergence of Equation (2) and using Equations (1) and (3), we have

$$\ddot{\delta} + 2H\dot{\delta} - 4\pi G\rho - \frac{\nabla^2 c_s^2 \delta}{a^2} = 0, \quad (6)$$

where the 3rd and the 4th terms correspond to the self-gravity and the pressure gradient of density perturbation, respectively. In the present context of our study, we consider the growth of fluctuations in the core of run-away collapsing gas cloud. Hence, we consider the

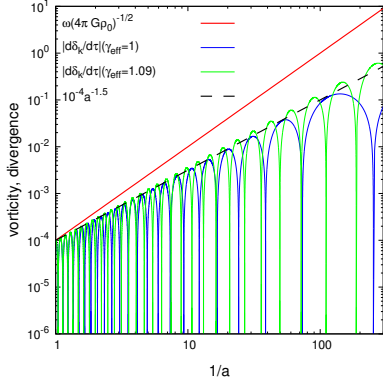


Figure 1. Growth of ω and $|d\delta_k/d\tau|$ is shown for $\kappa = 20$. Red: ω , Blue: $|d\delta_k/d\tau|$ for $\gamma_{\text{eff}} = 1$, Green: $|d\delta_k/d\tau|$ for $\gamma_{\text{eff}} = 1.09$. Dashed line shows $\propto a^{-1.5}$, which traces the amplitude of $|d\delta_k/d\tau|$.

scale below the core radius, which is identical to the Jeans scale. Thus, the 4th term is always larger than the 3rd term which results in the oscillation. The 2nd term behaves as a “negative drag” term, which causes the growth of density fluctuations, in contrast to the cosmological context.

In order to solve this equation, we need to define the collapsing background, $a(t)$. We assume that the core region of the runaway collapsing cloud grows in a self-similar fashion, thereby the density is given as $\rho(t) = 5/(12\pi G t^2)$ (Larson 1969; Suto & Silk 1988). Note that the origin of the time coordinate is taken when the density approaches infinity (the moment of the protostar formation). The scale factor $a(t)$ is related to the density as $\rho(t) = \rho_0 a(t)^{-3}$, where ρ_0 is the initial density at an initial time t_0 . After some algebra, Equation (6) is rewritten as

$$\frac{d^2\delta_k}{d\tau^2} + \frac{4}{3\tau} \frac{d\delta_k}{d\tau} - \frac{1}{a^3} (1 - \kappa^2 a^{1-3(\gamma_{\text{eff}}-1)}) \delta_k = 0 \quad (7)$$

where δ_k is the k -mode of density fluctuation, $\tau \equiv t\sqrt{4\pi G\rho_0}$ is the normalized time coordinate, $\kappa \equiv c_{s0}k/\sqrt{4\pi G\rho_0}$ is a normalized wave number, γ_{eff} is an effective polytropic index of barotropic equation of state, and c_{s0} denotes the sound velocity at $t = t_0$. According to the equation of continuity, $d\delta_k/d\tau$ denotes the divergence of the velocity field, which gives the compressive mode of the turbulence.

Figure 1 shows the growth of $|d\delta_k/d\tau|$ as functions of a^{-1} by integrating Equation (7) for $\gamma_{\text{eff}} = 1$ and 1.09. For larger a^{-1} we have higher density, which means that the system evolves from left to right. For simplicity, the initial condition is set as $\delta_k = 0, d\delta_k/d\tau = 10^{-4}$.

It is clear that $|d\delta_k/d\tau|$ oscillates and its amplitude increases as the density gets higher. This overstable behavior is expected, because of the presence of restitutive force term stems from the thermal energy as well as the

external force term by the gravitational contraction of the whole system. Note that the self-gravity term of the perturbation is not important for amplification, because we consider the region inside the collapsing core, thereby we only have to consider the scale less than the Jeans scale.

The amplitude of the oscillation grows as $\sim a^{-1.5}$ for $\gamma_{\text{eff}} = 1$ case, and slightly steeper for $\gamma_{\text{eff}} = 1.09$ (see the dashed line). This can be shown easily for $\gamma_{\text{eff}} = 1$ case, since the Equation (7) can be solved analytically for $\kappa \gg 1$. The general solution reads

$$\begin{aligned} \delta_k &= c_1 j_0(3\kappa(5\tau/3)^{1/3}) + c_2 n_0(3\kappa(5\tau/3)^{1/3}), \quad (8) \\ \frac{d\delta_k}{d\tau} &= -\kappa(5/3)^{1/3} \tau^{-2/3} \\ &\quad \times \left[c_1 j_1(3\kappa(5\tau/3)^{1/3}) + c_2 n_1(3\kappa(5\tau/3)^{1/3}) \right]. \quad (9) \end{aligned}$$

Here c_1 and c_2 are constants determined by the initial conditions, j_0, j_1, n_0, n_1 are the spherical Bessel functions. Utilizing the asymptotic form of $j_1(x) \simeq -x^{-1} \cos(x)$ and $n_1(x) \simeq -x^{-1} \sin(x)$ for $x \gg 1$ and Equation (9), we find that the amplitude of $d\delta_k/d\tau$ is proportional to $\tau^{-1} \propto a^{-1.5}$. Remark that this growth rate is less than that of the vorticity ω , as shown in Fig. 1.

Now we give analytic formulae for the amplification of velocity fluctuations. The solenoidal/compressive mode of the turbulent velocity at a given comoving scale $l = 2\pi/k$ is

$$v(l) = au \simeq \begin{cases} a\omega l \propto a^{-1}l & \text{solenoidal,} \\ a\dot{\delta} l \propto a^{-1/2}l & \text{compressive.} \end{cases} \quad (10)$$

We can regard $v(l)$ as the turbulent velocity.

As we can see in the above equations immediately, the compressive mode grows slower than the solenoidal mode. Hence the solenoidal mode dominates the compressive mode, as long as the initial amplitude of the two modes are at a same order of magnitude¹. In the line of this, we only consider the solenoidal mode below.

Since the turbulence consists of the flows with various scales in general, turbulent velocity should be obtained by summing up the contributions from all scales. In a most simple case, where l is the dominant scale of turbulence, and fixed in the course of the collapse, combining Equations (5), (10) and the relation $\rho \propto a^{-3}$, we obtain

$$v \propto \rho^{1/3}. \quad (11)$$

This indicates that the turbulent velocity increases as the gas contracts.

¹ Note that the expression of Equation (10) for the compressive mode is based upon the linear analysis. In case the solenoidal mode becomes much larger than the compressive mode, the non-linear term becomes important. In such a case, the growth of the compressive mode is boosted by the solenoidal mode.

In a realistic case, if the turbulence reaches to the Kolmogorov-like state, $v \propto l^{1/3}$ holds, which means that the turbulent velocity is larger for larger scales. The Jeans length is the core radius, which is the largest scale in the core at a given density. Hence, the Jeans length is the dominant scale. The Jeans length in the comoving frame is given as:

$$l_J \equiv \frac{1}{a} \left(\frac{\pi c_s^2}{G\rho} \right)^{1/2} \propto \rho^{(3\gamma_{\text{eff}}-4)/6} \quad (12)$$

Using Equations (10) and (11) on the scale given by $l = l_J$, we may obtain the turbulent velocity at l_J , but we still need an additional factor. We need to multiply a factor which comes from the intrinsic shape of the spectrum. If we assume the turbulent energy spectrum $E(k) \propto k^{-2\alpha-1}$, the total energy for $k > k_J$ is

$$\epsilon(k > k_J) = \int_{k_J}^{\infty} E(k) dk \propto k_J^{-2\alpha} \quad (13)$$

where k_J equals to $2\pi/l_J$, i.e., Jeans scale at a given time. Using Equations (10), (12), (13) and $v = \sqrt{2\epsilon}$ we have

$$v \propto \rho^{1/3} l_J^\alpha \propto \rho^{(3\gamma_{\text{eff}}-4)\alpha/6+1/3}. \quad (14)$$

For instance, substituting $\gamma_{\text{eff}} = 1$ (isothermal) and $\alpha = 1/2$ (Larson's law) in the above expression, the exponent becomes $1/4$, and thus the turbulent velocity slowly increases during the collapse.

Assuming α to be constant, the above relation can be interpreted to the condition that the required initial Mach number ($\mathcal{M}_{0,\text{cr}}$) at ρ_0 for the turbulent velocity to be amplified to the level of sound speed at a given density (ρ_{sonic}):

$$\mathcal{M}_{0,\text{cr}} = \left(\frac{\rho_0}{\rho_{\text{sonic}}} \right)^{((3\gamma_{\text{eff}}-4)\alpha+5-3\gamma_{\text{eff}})/6}. \quad (15)$$

If we employ $\gamma_{\text{eff}} = 1.09$ and $\alpha = 1/2$, the critical Mach number is ~ 0.001 for $\rho_0 = 10^{-19} \text{ g cm}^{-3}$ and $\rho_{\text{sonic}} = 10^{-6} \text{ g cm}^{-3}$. Considering the initial turbulence of $\mathcal{M}_{0,\text{cr}} \sim 0.001$ can be easily achieved by accretion flows onto minihalos (e.g. Greif et al. 2012), these analytic estimation suggests that the turbulent velocity in the collapsing core should be account for at least the level of the sound speed when the density approaches to the protostellar density.

3. NUMERICAL METHOD

We use the *N*-body/adaptive mesh refinement (AMR) cosmological hydrodynamic simulation code *Enzo* (Bryan et al. 2014)² to solve the gas contraction and growth of turbulence. This code solves the

compressive hydrodynamic equations with the Piecewise Parabolic Method (PPM) in an Eulerian frame while using a HLLC Riemann solver.

We use a simplified polytropic model,

$$P \propto \rho^{\gamma_{\text{eff}}}, \quad (16)$$

where P is the gas pressure. Initially, we set the uniform gas temperature $T_0 = 200 \text{ K}$ and the mean molecular weight $\mu_0 = 1.22$. In order to test Equation (14), we perform simulations with various polytropic indices of

$$\gamma_{\text{eff}} = \begin{cases} 1.2, \\ 1.09 \quad (\text{primordial}), \\ 1.0 \quad (\text{isothermal}). \end{cases} \quad (17)$$

The model with $\gamma_{\text{eff}} = 1.09$ mimics the collapse of the primordial gas (Omukai & Nishi 1998).

The initial condition is an isothermal Bonnor-Ebert sphere with an initial peak density $\rho_{\text{peak},0} = 4.65 \times 10^{-20} \text{ g cm}^{-3}$ which mimics a collapsing primordial gas cloud in the ‘‘loitering’’ phase. To boost the contraction, the density of the Bonnor-Ebert sphere is uniformly enhanced by a factor $f = 1.35$ (Matsumoto & Hanawa 2011). The radius r_c of the cloud is 1.5 pc, and the size of the computational domain is $L_{\text{box}} = 5 \text{ pc}$. Then, we add the turbulent velocity field. The velocity power spectrum of turbulence is given by the Larson's law $P(k) \propto k^{-4}$ at a wavenumber k . Hence the kinetic energy spectrum $E(k) \propto k^2 P(k)$ is proportional to k^{-2} (Dubinski et al. 1995; Matsumoto et al. 2015). We assume the initial root-mean-square Mach number $\mathcal{M}_0 = 0, 0.005, 0.01, 0.05, \text{ and } 0.1$. These low Mach numbers are employed because we try to understand the amplification by the gravitational contraction. We do not explicitly give the rotational velocity to focus only on the effects of the turbulent velocity field, although the turbulence introduces a small amount of angular momentum.

Enzo's AMR technique allows us to follow the gas contraction over a wide dynamic range. We start the calculations with a base grid with 256^3 computational cells. We progressively refine cells as the gas cloud collapses so that the Jeans length is always resolved by at least 128 cells. Hereafter, the minimum number of cells account for the Jeans length is called as the Jeans Parameter. The initial conditions are summarized in Table 1.

In order to investigate the resolution dependence of the amplification of the turbulence, we also run simulations for different numbers of cells on the base grid and Jeans Parameters for $\gamma_{\text{eff}} = 1.09$. These models with different base grid sizes and Jeans Parameters are called as RM32–RM512 (Table 2). We conduct RM512 only for $\mathcal{M}_0 = 0.05$ in order to save the computational cost.

We terminate the simulations when the peak density exceeds $10^{-4} \text{ g cm}^{-3}$ for all models. We use the YT

² <http://enzo-project.org/>

Table 1. Initial parameters

Parameters	Initial values
Central density	$4.65 \times 10^{-20} \text{ g cm}^{-3}$
Velocity power spectrum	$\propto k^{-4}$
Mach Number	0, 0.005, 0.01, 0.05, 0.1
Temperature	200 K
Mean molecular weight	1.22
Polytropic index	1.2, 1.09, 1.0
Base grid	256^3
Jeans Parameter	128

Table 2. Parameters for resolution study

Polytropic index		
1.09		
Model	Base Grid	Jeans Parameter
RM32	32^3	16
RM64	64^3	32
RM128	128^3	64
RM256	256^3	128
RM512	512^3	256

Note: The other parameters are same as Table 1.
RM512 is only for $\mathcal{M}_0 = 0.05$.

toolkit (Turk et al. 2011)³ to analyze the data for all simulations.

4. RESULTS

4.1. Overall density structure

Figure 2 shows the density-weighted density projection plots (upper panel) and radially averaged profiles of the density (lower panel) for the model with $\mathcal{M}_0 = 0.1$ when peak density reaches $10^{-4} \text{ g cm}^{-3}$. The self-similar evolution of the gas cloud forms the core-envelope structure in the density distribution. The density-radius relation in the envelope is consistent with the analytic expression $\rho \propto r^{-2/(2-\gamma_{\text{eff}})}$ (Suto & Silk 1988), as shown in the lower panel.

We can see the disturbed density fields and deformation of the gas clouds for $\gamma_{\text{eff}} = 1.09$ and 1.0, while the density distribution is less fluctuated and spherical for $\gamma_{\text{eff}} = 1.2$. This is due to the gravitational instability of the system for cloud deformation. These results are consistent with the semi-analytic studies, which show bar-mode perturbations grow on spherically collapsing clouds with $\gamma_{\text{eff}} < 1.097$ (Hanawa & Matsumoto 2000; Lai 2000).

Figure 3 shows the evolution of the mean density of the core as a function of time $-t$ for $\mathcal{M}_0 = 0.1$ and $\gamma_{\text{eff}} = 1.09$. Here the origin of the time coordinate is

at the time of final snapshot, which approximately represents the time when the core density diverges in the similarity solution. The mean density ρ_{mean} is calculated in a spherical region with a radius $L_J/2$ (hereafter called ‘‘Jeans volume’’) of every snapshot. Here L_J is the Jeans length in the proper coordinate.

We can clearly see the mean density evolves following the relation $\rho_{\text{mean}} = \frac{5}{12\pi G} t^{-2}$. This again agrees with the Larson-Penston type similarity solution for a gravitationally contracting polytropic sphere (Suto & Silk 1988). These results support our assumption for the analytic estimate in Section 2.

4.2. The growth of turbulence

We calculate the average turbulent velocity in the Jeans volume. The turbulent velocity v_{turb} is defined as

$$v_{\text{turb}}^2 \equiv \sum_{\leq L_J/2} \frac{V_i}{V_J} (\mathbf{v}_i - \mathbf{v}_{\text{rad},i})^2, \quad (18)$$

where V_i is the volume of the i ’th cell, and V_J is the Jeans volume. It is difficult to estimate the *unperturbed* radial velocity $\mathbf{v}_{\text{rad},i}$ at the position of each cell i because the velocity fluctuation is contaminated with the background radial velocity in the simulation data. We guess the background radial velocity to estimate the turbulent velocity field by means of the following procedure: First, we calculate the radial velocity profile with N_{rad} radial bins. N_{rad} should be smaller than the Jeans parameter so that we can remove the velocity fluctuations at the scale of the cell size. Here, we set $N_{\text{rad}} = 16$. Second, we linearly interpolate this profile to estimate the smoothed radial velocity $\mathbf{v}_{\text{rad},i}$ at the position of each cell. Third, we subtract $\mathbf{v}_{\text{rad},i}$ from the total velocity \mathbf{v}_i of the cell to extract the component of the fluctuation. Finally, we calculate the cell volume-weighted average of the turbulent velocity among cells in the Jeans volume according to Equation (18). We use the ‘volume-weighted’ average instead of the ‘mass-weighted’ average here. We do not find any significant difference between the results from the two methods because we are now considering only the central part of the gas cloud, where the density inhomogeneity is not so large even in the isothermal model ($\sqrt{\langle \delta^2 \rangle} \lesssim 0.9$). We will discuss the density fluctuation in section 4.4 and in Figure 11.

Since the mean density ρ_{mean} of the Jeans volume almost monotonically increases, we can show the temporal evolution of the turbulent velocity v_{turb} as a function of ρ_{mean} of every snapshot in Figure 4. In all models, the turbulent velocity increases as the density increases through the contraction. Similarly, Figure 5 shows the evolution of the vorticity as a function of the mean density for various initial Mach numbers. In all models, the vorticity increases monotonically with the increasing density.

In these figures, for $\mathcal{M}_0 \geq 0.05$, we can see that Equation (14) and Equation (5) are in good agreement with

³ <https://yt-project.org/>

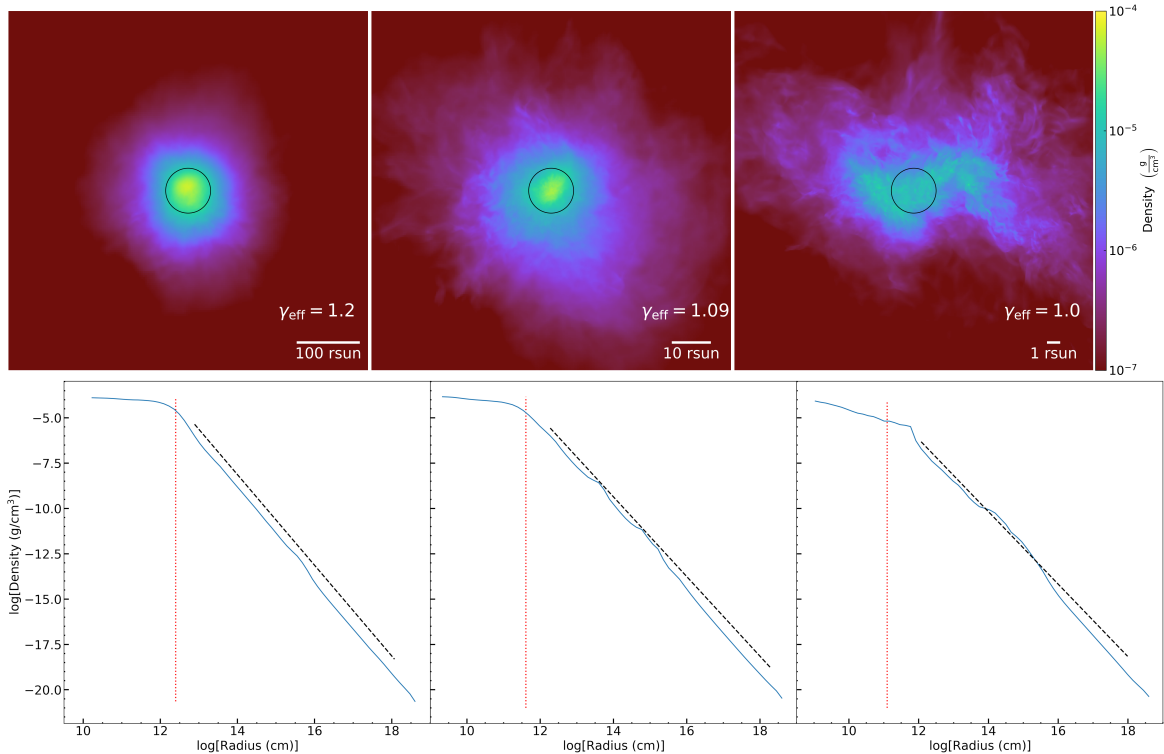


Figure 2. Density-weighted density projection plots (upper panel) and radially averaged profiles of the density (lower panel) for the model with $\mathcal{M}_0 = 0.1$ when the peak density reaches $10^{-4} \text{ g cm}^{-3}$. In the upper panel, side length of each plot is set to $8L_J$ and the black circles have a radius of $L_J/2$. The red dotted lines in the lower panel indicate $L_J/2$. The black dashed lines in the lower panel denote $\propto r^{-2/(2-\gamma_{\text{eff}})}$, where r is the radius from the center of the gas clouds.

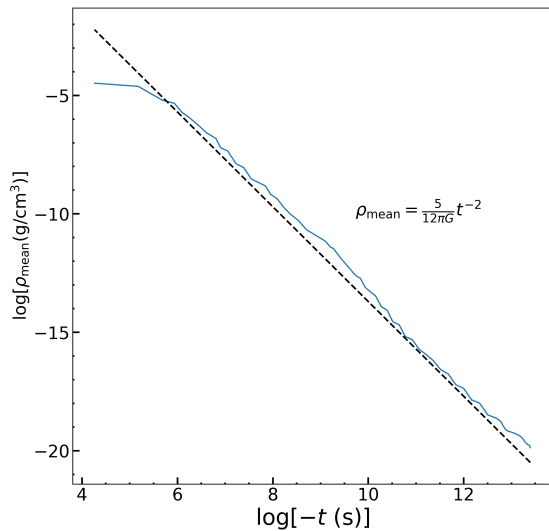


Figure 3. Evolution of the mean density of the core as a function of time for $\mathcal{M}_0 = 0.1$ and $\gamma_{\text{eff}} = 1.09$. A black dashed line corresponds to $\rho_{\text{mean}} = \frac{5}{12\pi G} t^{-2}$.

the numerical results for all γ_{eff} before they reach the sound velocity. We also find that all models with $\mathcal{M}_0 \geq 0.05$ reach to the transonic/supersonic points before it reaches the protostellar density ($\rho_{\text{peak}} \gtrsim 10^{-4} \text{ g cm}^{-3}$). Hence, the run-away collapsing core will easily achieve

the turbulent velocity of $\sim c_s$, even with a weak initial turbulence. In fact, \mathcal{M}_0 of these models is larger than the threshold Mach number shown in Equation (15) for $\rho_{\text{sonic}} = 10^{-6} \text{ g cm}^{-3}$ and $\rho_0 = 4.65 \times 10^{-20} \text{ g cm}^{-3}$. Considering the good match with the theory in Section 2 with the numerical results, this is a good evidence that the turbulent velocity is amplified via adiabatic heating associated with the gravitational contraction.

It is worthy to note that the turbulent velocity is saturated at $\sim c_s$ for $\gamma_{\text{eff}} = 1.2$ models, whereas it reaches well above the sound velocity in other two models (Figure 4). These results naturally explain the presence of supersonic turbulence in the first star forming core in cosmological simulations (e.g. Greif et al. 2012). In Figure 5, we also find the sign of saturation for all γ_{eff} for $\mathcal{M}_0 \geq 0.05$. The vorticity after the saturation roughly obeys $\omega \propto \rho_{\text{mean}}^{1/2}$, which is predicted by Robertson & Goldreich (2012). They also have shown that uniformly contracting isothermal gas ($\gamma_{\text{eff}} = 1$) with initially supersonic turbulence ($\mathcal{M}_0 = 6$) can reach as high as $\mathcal{M} = 11.2$. This Mach number is much higher than that is found in our simulations. We guess the main reason of this difference is that they did not solve the gravitational collapse, but we do. They mimic the collapse by increasing the average density at a given rate by hand, like ‘‘collapsing universe’’. In our calculation, the cloud core size shrinks as the collapse proceeds, so

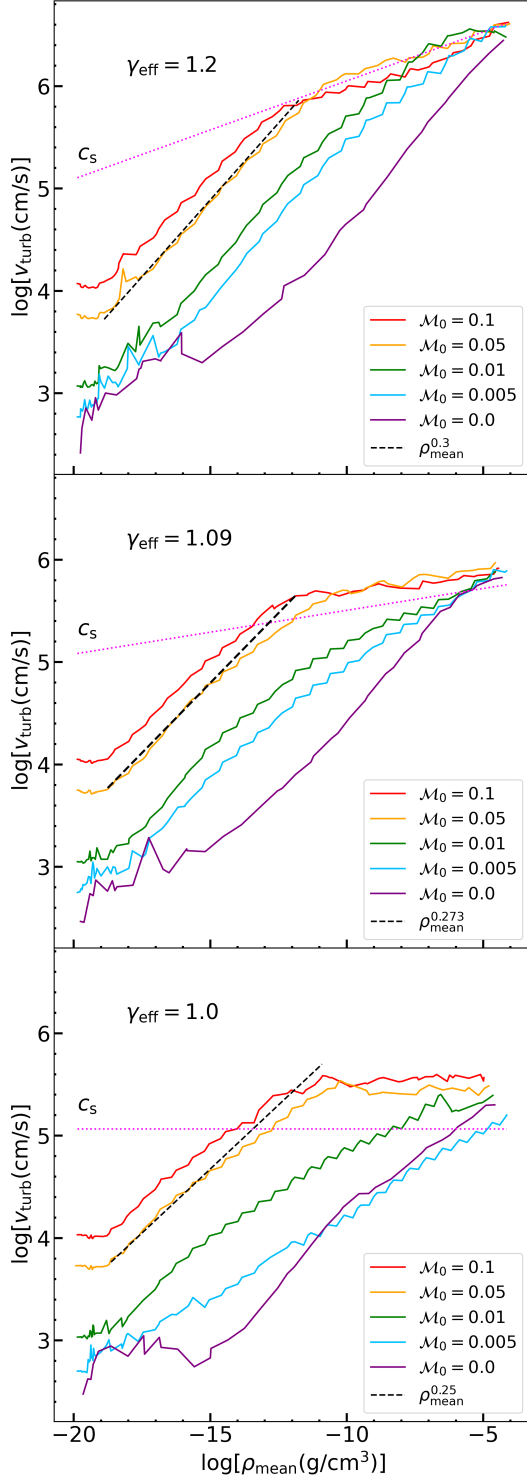


Figure 4. Evolution of the turbulent velocity v_{turb} as a function of mean density ρ_{mean} in a spherical region centered on the density mean with a radius of half of the Jeans length (Jeans volume) for $\gamma_{\text{eff}} = 1.2$ (top panel), 1.09 (middle panel), and 1.0 (bottom panel). The solid curves with different colors denote the numerical results for different initial turbulent Mach numbers \mathcal{M}_0 . The magenta dotted line denotes the average sound speed in the Jeans volume. The black dashed lines depict our analytic estimates (Equation 14).

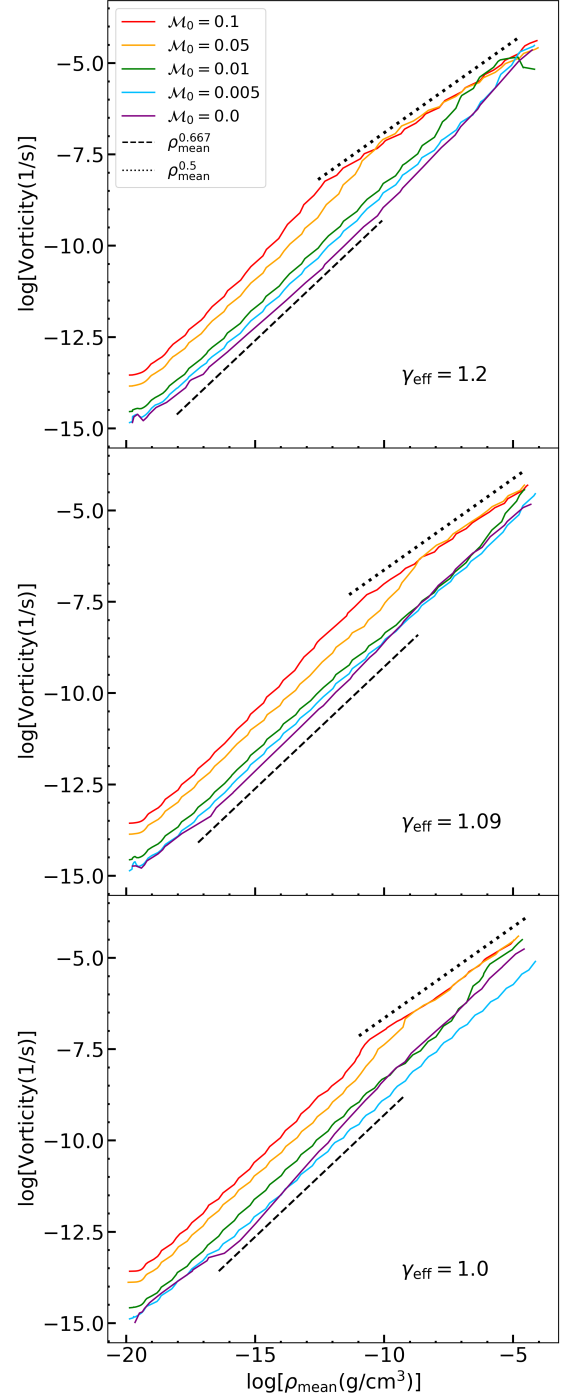


Figure 5. Evolution of the vorticity as a function of the mean density for $\gamma_{\text{eff}} = 1.2$ (top panel), 1.09 (middle panel), and 1.0 (bottom panel). The solid curves denote the numerical results of each \mathcal{M}_0 . The black dashed line is our analytic estimate (Equation 5). The black dotted line denotes $\propto \rho_{\text{mean}}^{0.5}$.

we guess the decrease of the forcing scale (the core size, L_J in our case) causes the higher dissipation rate of turbulence (see eq. 7 in Mac Low (1999)). We speculate this rapid dissipation avoids highly supersonic turbulent flows.

For $\mathcal{M}_0 \leq 0.01$, the turbulent velocity oscillates around $\sim 0.01c_s$ at the early stage of the collapse, ($\rho_{\text{mean}} < 10^{-15} \text{ g cm}^{-3}$) as shown in Figure 4. As will be discussed in Section 4.5, this behavior implies that the turbulent velocity at this stage is contaminated by the numerical error introduced by the Cartesian grid. The initial seed velocity field is so weak that it is hidden among the added errors due to grid discretization. After this early stage, as the eddies being resolved, the turbulent velocity turns to increase even slightly faster than the cases for $\mathcal{M}_0 \geq 0.05$, roughly proportional to $\rho_{\text{mean}}^{1/3}$. This may be due the flattening of the energy spectrum around the Jeans scale. This point will be discussed in Section 4.3. Finally, the turbulent velocities in all models reaches to the order of sound velocity. However, as mentioned above, the turbulent velocity in the models of $\mathcal{M}_0 \leq 0.01$ are floored by numerical errors. Hence these results seems to be a numerical artifact. On the other hand, the initial Mach number of these models except $\mathcal{M}_0 = 0.0$ exceeds the critical number described as Equation (15). Thus, it is expected that these models will achieve the transonic/supersonic turbulence even if enough resolution is provided.

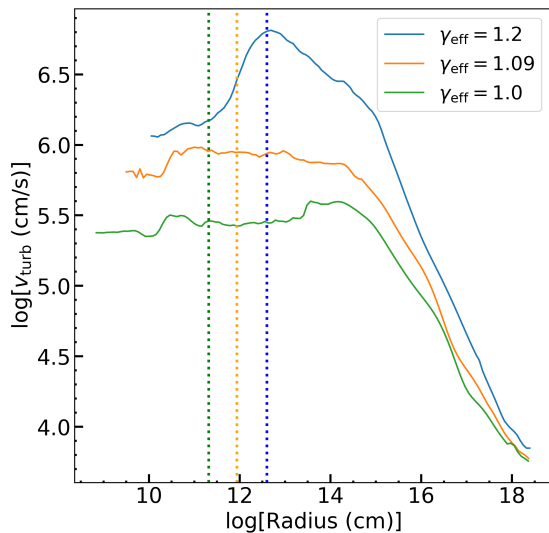


Figure 6. Radial profiles of turbulent velocity averaged over the shell of radial bins with $\mathcal{M}_0 = 0.05$ for each γ_{eff} when the peak density reaches $10^{-4} \text{ g cm}^{-3}$. The vertical lines correspond to the half of Jeans length for each γ_{eff} .

We also plot the radial profiles of turbulent velocity averaged over the shell of radial bins as a function of radius from the center of mass of the cloud in Figure 6. This plot is for $\mathcal{M}_0 = 0.05$. Since the turbulent velocity

increases with contraction, it exhibits a core-envelope structure as the density distribution shows. In the core region, the turbulence is saturated, and its amplitude seems to be determined by the saturation level (Figure 4). The saturation occurs at densities $\sim 10^{-8} \text{ g/cm}^3$, much smaller than the peak density. Therefore, the core radius in the turbulent velocity profile is larger than the core in the density profile. We also find that the radial profile tends to drop towards the cloud center. We do not understand the actual reason of this drop, but the profile of $\gamma_{\text{eff}} = 1.09$ is more or less consistent with Fig.1 in Federrath et al. (2011) who employ $\gamma_{\text{eff}} = 1.1$.

Figure 7 shows the evolution of gravitational, kinetic, turbulent, and thermal specific energies as a function of mean density.

Here, ‘turbulent energy’ means the kinetic energy minus the energy of bulk radial motion. We define each specific energy to compare in the same units as follows:

$$E_{\text{grav}} \equiv \left| -\frac{3}{5} \frac{GM_J}{L_J/2} \right|, \quad E_{\text{kin}} \equiv \frac{1}{2} v^2,$$

$$E_{\text{turb}} \equiv \frac{1}{2} v_{\text{turb}}^2, \quad E_{\text{th}} \equiv \frac{1}{\gamma_{\text{ad}} - 1} \frac{k_B T}{\mu m_H}.$$

Here, M_J , γ_{ad} , k_B , and m_H are mass within the Jeans length, the specific heat ratio of the gas, Boltzmann constant, and hydrogen mass, respectively.

To calculate the thermal energy we assume γ_{ad} to 5/3 because we do not solve chemical reactions in this work. The factor 3/5 in E_{grav} comes from the approximation that the core is uniform. E_{kin} , E_{turb} and E_{th} are evaluated as the cell volume weighted averages, again with the uniform core approximation. For $\gamma_{\text{eff}}=1.0$, the kinetic and turbulent energies increase until they are comparable to the gravitational energy, while in the other models they increase but do not reach that level. The detailed physical mechanism of saturation and the dependence of the saturation level on γ_{eff} are interesting, but they are out of scope of this work. We will address these issues in our future study.

4.3. Solenoidal/Compressive modes

The turbulent field is composed of solenoidal and compressive modes. The divergence free velocity fields corresponds to the solenoidal mode, and the rotation free fields are compressive. As we discussed in Section 2, the turbulent velocity which is amplified by the contraction is accompanied by vorticity and divergence. Thus, it is interesting that which mode is dominant for the amplification of the turbulence. We study this point in this section. We are also interested in the energy spectrum, because Equation (14) critically depends on the assumption that spectrum is described by a constant single power law index α , which equals to 1/3 for Kolmogorov turbulence and equals to 1/2 for Larson’s law. In this section, we focus on the results in the model of $\gamma_{\text{eff}} = 1.09$.

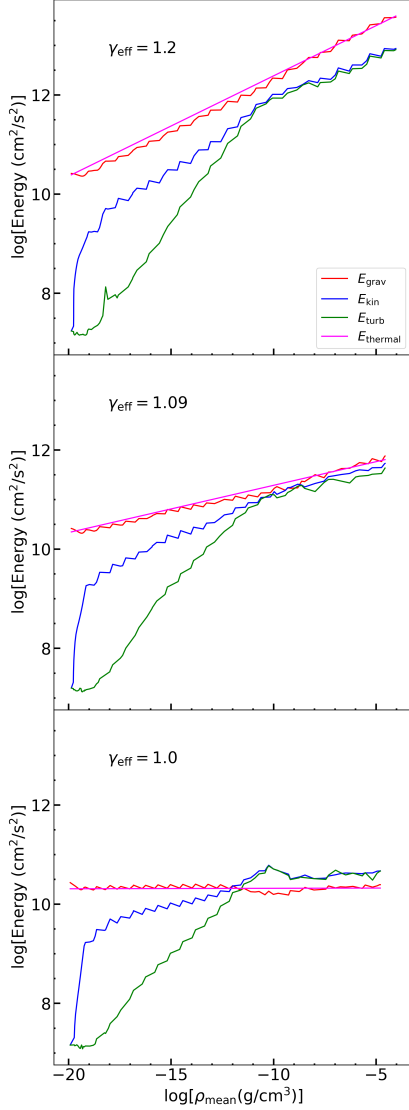


Figure 7. Evolution of the specific energy for $\mathcal{M}_0 = 0.05$ as a function of the mean density for $\gamma_{\text{eff}} = 1.2$ (top panel), 1.09 (middle panel), and 1.0 (bottom panel). Red, blue, green, and magenta lines denote the gravitational, kinetic, turbulent, and thermal specific energies, respectively.

We compute the velocity in Fourier space (hereafter k -space) on a uniform grid compatible with the highest refinement level, using a fast Fourier transform with a window of the spherical Bessel function in the cube of L_J on one side. The reason why we use the window function is to suppress the “side-lobe” caused by the non-periodic boundary condition of the cube. Applying the Helmholtz decomposition, we can decompose the obtained velocity field into solenoidal modes $\hat{v}_{\text{sol}}(k)$ and the compressive modes $\hat{v}_{\text{comp}}(k)$ in k -space as

$$\begin{aligned}\hat{v}_{\text{comp}}(\mathbf{k}) &= (\mathbf{k} \cdot \hat{v}(\mathbf{k}))\mathbf{k}/k^2, \\ \hat{v}_{\text{sol}}(\mathbf{k}) &= (\mathbf{k} \times \hat{v}(\mathbf{k})) \times \mathbf{k}/k^2,\end{aligned}\quad (19)$$

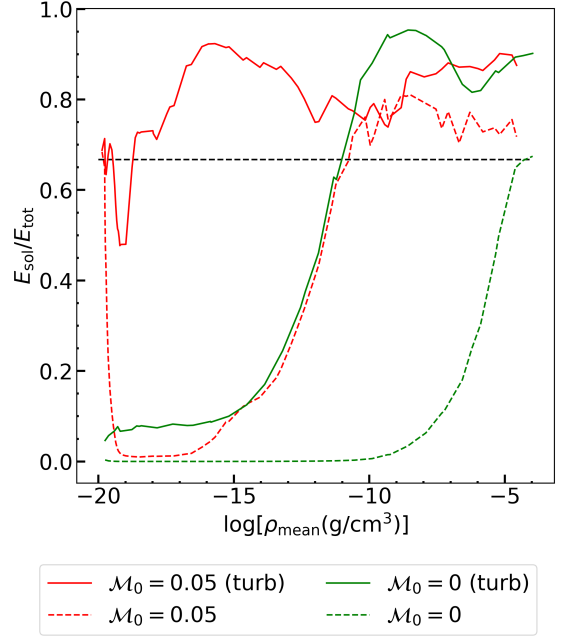


Figure 8. Evolution of the solenoidal ratio as a function of the mean density. The solid lines denote the solenoidal ratio of the turbulent velocity for each model of \mathcal{M}_0 . The dashed lines are the same as the solid lines, but the cases of the total velocity. The black dotted line corresponds to the natural mixture ratio. $\gamma_{\text{eff}} = 1.09$ in every model.

where $\hat{v}(\mathbf{k})$ is the velocity in k -space and \mathbf{k} is the wave vector. The minimum wavenumber corresponds to the spatial scale of half of the Jeans length. Then, we calculate the kinetic energy of each mode as

$$\begin{aligned}E_{\text{comp}} &= \int_{k_J}^{\infty} \hat{E}_{\text{comp}}(k) dk \equiv \frac{1}{2k_J^3} \int_{k_J}^{\infty} |\hat{v}_{\text{comp}}(\mathbf{k})|^2 4\pi k^2 dk, \\ E_{\text{sol}} &= \int_{k_J}^{\infty} \hat{E}_{\text{sol}}(k) dk \equiv \frac{1}{2k_J^3} \int_{k_J}^{\infty} |\hat{v}_{\text{sol}}(\mathbf{k})|^2 4\pi k^2 dk.\end{aligned}\quad (20)$$

First, we show the growth of the energy of solenoidal mode in Figure 8. We define the solenoidal ratio as $E_{\text{sol}}/E_{\text{tot}}$ where E_{tot} is the sum of solenoidal and compressive modes. The black dotted line in Figure 8 shows the solenoidal ratio for the natural mixture. As discussed in Federrath et al. (2011), this natural ratio $\sim 2/3$ can be approximated to be the number ratio of the modes of longitudinal waves which induce the rotational motion of the gas in a three-dimensional system. The dashed curves of Figure 8 show the total velocity including the bulk motion, whereas the solid curves denotes the turbulent velocity subtracted the radial infall $\mathbf{v}_{\text{rad},i}$ defined in Section 3. For the model with $\mathcal{M}_0 = 0.05$, the solenoidal ratio is initially close to 0.67, because we initially set the velocity field with the natural mixture. In this case, the solenoidal ratio of the turbulent component (solid curves) increases up to ~ 0.9 after the collapse begins, and maintains its high value until the

end of collapse. This is because the growth rate of the solenoidal mode is larger than that of the compressive mode. In short, for model $\mathcal{M}_0 = 0.05$, the turbulence is dominated by the solenoidal mode, while it is growing.

In contrast to this case, the solenoidal ratio is relatively low in the low-density region for the model with $\mathcal{M}_0 = 0$. This behavior suggests that the numerical error introduced in the low density region is basically the compressive mode. This is reasonable, because the error accrues concomitant with the radial converging flow. As the collapse proceeds, the solenoidal ratio reaches ~ 0.9 in the high-density region as well as for $\mathcal{M}_0 = 0.05$ (green and red solid curves). This means that the launch of the growth of solenoidal mode is delayed for $\mathcal{M}_0 = 0$, but eventually overwhelms the compressive mode.

For the kinetic energy including the radial inflow velocities (dashed curves), the solenoidal ratio decreases rapidly after the onset of collapse, and almost close to zero in the both cases. As the gas collapses, the solenoidal ratio gradually increases due to the amplification of the solenoidal modes, and eventually converges to the natural mixture, which is consistent with the results of Federrath et al. (2011).

Next we show six snapshots of the energy spectrum in Figure 9. Left panels show the solenoidal mode, and the right panels show the compressive mode. Upper and lower row denote the $\mathcal{M}_0 = 0.05$ and $\mathcal{M}_0 = 0$ models, respectively. The different colors indicate different values of ρ_{mean} . The horizontal axes show the wave number normalized by the Jeans scale at the corresponding mean density.

For $\mathcal{M}_0 = 0.05$, the solenoidal mode roughly keeps a power law energy distribution. Initially, it is set as $\propto k^{-2}$ and the slope at small k end ($< 5k_J$) keeps $\propto k^{-2}$.

It is also important that E_{sol} basically a few–10 times larger than E_{comp} at each snapshot.

On the other hand, for $\mathcal{M}_0 = 0$ model, compressive mode dominates initially, although no turbulence is added by hand.⁴ This is obviously the error introduced by discretization, that should accompany the radial inflow. As the collapse proceeds, the solenoidal mode takes over the compressive mode at $\rho_{\text{mean}} \gtrsim 10^{-11} \text{ g cm}^{-3}$. The initial growth of solenoidal mode (bottom 3–4 curves) is remarkable, that seems to be boosted by the large compressive mode. The boost by the compressive mode ends earlier for smaller k eddies and the growth becomes slower. This is because E_{sol} for small k mode is larger than that of large k modes, to overtake the compressive mode earlier. As a result, E_{sol} for larger k mode are able to catch up that of smaller k modes. This effect causes the flattening of the spectrum of E_{sol} , which we observe in the spectrum from the

second (blue) to fourth (green) snapshots. In particular, the low k end of the fourth snapshot is nearly flat. This means $\alpha \simeq 0$ in Equation (14) to have $v \propto \rho^{1/3}$ for $\gamma_{\text{eff}} = 1.09$. This trend is already observed in the middle panel of Figure 4. However, as we already have mentioned, this growth relies on the presence of the numerical error in the compressive mode. Hence this should be regarded as a numerical artifact.

As discussed in the previous paragraph, mode coupling between the solenoidal mode and the compressive mode plays important roles. To show the effects of the mode coupling during the turbulence amplification in detail, we plot each mode of turbulence for $\mathcal{M}_0 = 0.05$ as a functions of density (Figure 10). According to Equation (10), the compressive mode of the turbulent velocity is expected to grow slower than the solenoidal mode.

However, we can observe that the compressive mode of the turbulent velocity grows at a similar growth rate to that of the solenoidal mode, although it does not increase in the very early phase. Considering the fact that the growth rate of the compressive mode in the linear analysis is smaller than that of the solenoidal mode (Equation 10), it is reasonable to regard that the energy conversion from the solenoidal mode to the compressive mode does occur. This should result from the nonlinear term of the equation of motion of the hydrodynamics. As a result, the amplitude of the compressive mode is a few times smaller than that of the solenoidal mode in this calculation throughout the collapse.

4.4. Density fluctuations

In order to understand more about the compressive mode, we investigate density fluctuations in the core, which is directly related to the compressive turbulence. We plot density fluctuations (Figure 11) as a function of density ρ_{mean} for $\mathcal{M}_0 = 0.1$. Here the density fluctuation is defined as

$$\langle \delta^2 \rangle \equiv \sum_{\leq L_J/2} \frac{V_i}{V_J} \left(\frac{\rho_i - \rho_{\text{rad},i}}{\rho_{\text{rad},i}} \right)^2, \quad (21)$$

where V_i is the volume of the i 'th cell, and V_J is the Jeans volume. ρ_i is the density of the i 'th cell, $\rho_{\text{rad},i}$ denotes the density averaged in each radial shell where i 'th cell is included. We set the number of radial bins N_{rad} to be 16 in the Jeans Volume as we did for turbulent velocity.

We can observe the oscillations of root-mean-square density fluctuations in the core. This oscillation may be due to the overstable behavior of the compressive modes of turbulence.

We also notice that the density fluctuations in all γ_{eff} grow initially, but the growth is stopped around $\rho_{\text{mean}} \sim 10^{-12} \text{ g/cm}^3$, where the saturation of turbulence occurs (Figure 4). As a result, density fluctuations do not grow to the level of $\gg 1$, although they vary $\sim 0.1 - 0.9$ after the saturation depending on γ_{eff} . These behavior could

⁴ Note that this earliest snapshot corresponds to the time slightly after the start of the simulation, not at exactly the beginning of the calculation.

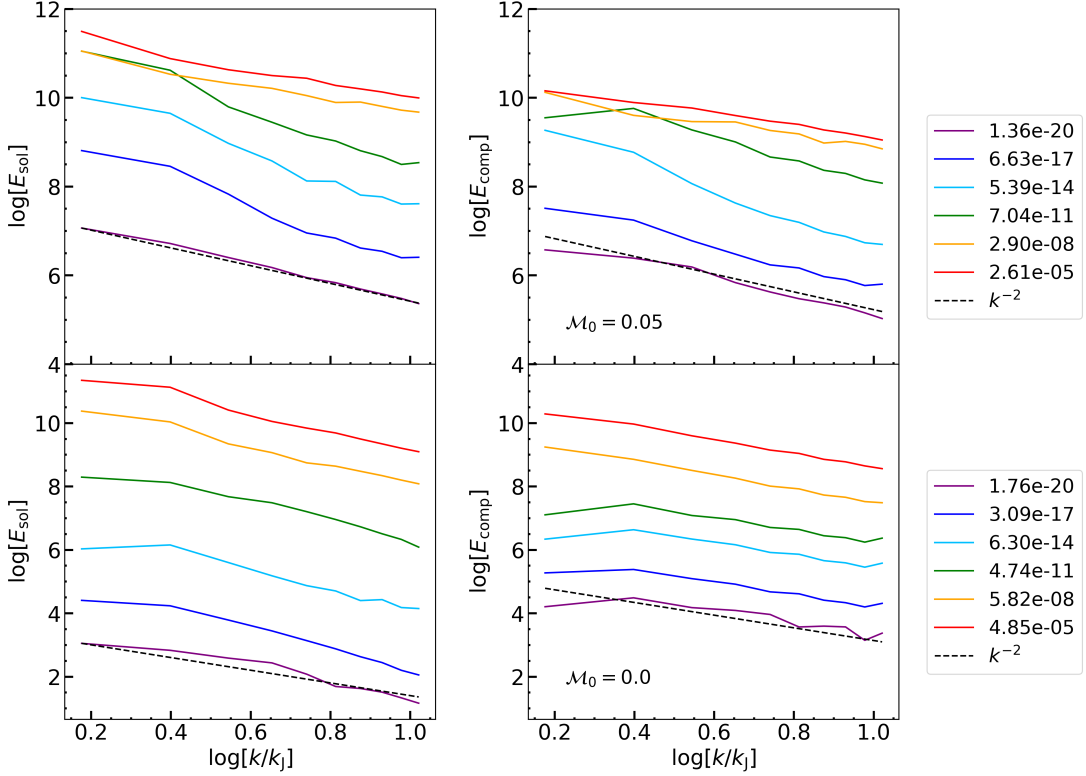


Figure 9. Evolution of the turbulent kinetic energy spectra of solenoidal modes (left column) and compressive modes (right column) for $\mathcal{M}_0 = 0$ (upper row) and 0.05 (lower row), respectively. The solid curves show the numerical results. The dashed curves show reference power-law spectra $\propto k^{-2}$, indicating the scaling relations of the Larson’s law turbulence. The different colors indicate different values of ρ_{mean} .

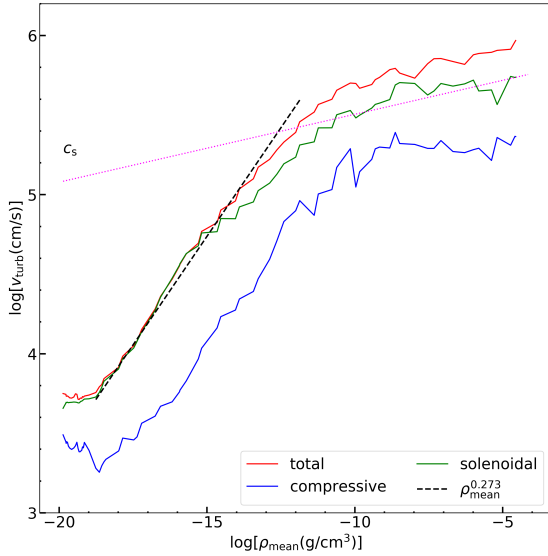


Figure 10. Evolution of each modes of the turbulent velocity as a function of the mean density for $\mathcal{M}_0 = 0.05$ and $\gamma_{\text{eff}} = 1.09$. Red, green, and blue solid lines correspond to the total, solenoidal, compressive modes of the turbulent velocity.

be roughly explained in analytic way. As discussed in the previous paragraph, the compressive mode grows at the rate of the solenoidal mode due to the mode coupling. This means $\dot{\delta} \sim \omega \propto a^{-2}$ in the light of Equation (10). Consequently, we have $\delta \propto (-t)^{-4/3}$, thus $\delta \propto (-t)^{-1/3} \propto \rho^{1/6}$. This is the reason for the initial gradual growth of the density fluctuation. After the saturation, growth rate of the vorticity changes as $\omega \propto \rho^{1/2}$. This results in a relation $\delta \propto \ln(-t)$, thus the growth is stopped after saturation.

4.5. Noise induced by the Discretization

Here, we describe the error introduced by the discretization. In order to understand the nature of the numerical errors, we perform resolution studies. Figure 12 shows the velocity field (arrows) overlotted on the density slice (color scales) of the x-y plane containing the domain center at $t = 100$ kyr corresponding to $\rho_{\text{mean}} \sim 1.8 \times 10^{-20} \text{ g cm}^{-3}$. Four panels show the results of RM256–RM32 models without the initial turbulence ($\mathcal{M}_0 = 0$). These snapshots correspond to a very early phase of the collapse when the central density increases only by $\sim 5\%$ from the initial density. The gas clouds will collapse in a spherically symmetric manner if we have an infinite resolution, and the velocity should have only a radial component without any initial turbu-

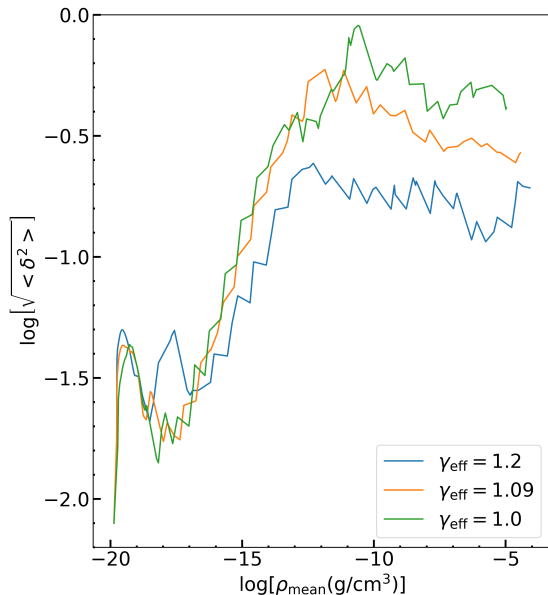


Figure 11. Evolution of density fluctuations as a function of mean density for $\mathcal{M}_0 = 0.1$. The different colors correspond to different γ_{eff} .

lence. However, we can see that non-radial components of velocity fields exist, and RM32 has larger noises than RM256. This stems from the Cartesian structure of the grid, and this disturbance is the seeds of velocity fluctuations in this $\mathcal{M}_0 = 0$ models.

Figure 13 shows v_{turb}^2 at $t = 100$ kyr corresponding to $\rho_{\text{mean}} \sim 1.8 \times 10^{-20} \text{ g cm}^{-3}$ as a function of the cell size normalized by the box size.

We plot v_{turb}^2 with open circles for each resolution model for $\mathcal{M}_0 = 0.05$ (upper panel) and $\mathcal{M}_0 = 0.0$ (lower panel) to measure the amplitude of the numerical noise. In order to assess the dependence of the noise on the resolution, we obtain the power law fitting function (red dotted lines) with a least-square method.

As a result, for $\mathcal{M}_0 = 0.05$ there is no resolution dependence so that the turbulence of these models is not affected by the numerical error, while we find the fitted function is proportional to (cell width) $^{1.8}$ for $\mathcal{M}_0 = 0.0$. The dependence on the cell width for $\mathcal{M}_0 = 0.0$ means that the error is the second order. In absence of the initial turbulence, the specific energy of the turbulence ($\sim v_{\text{turb}}^2$) at the very early stage could be introduced by the transformation of the aspherically symmetric component of the gravitational potential. In fact, Enzo’s gravitational potential solver is a second-order accurate (James 1977; Bryan et al. 2014). Thus, it is reasonable that v_{turb}^2 shows a resolution dependence that is proportional to almost the square of the cell width.

Figure 14 shows the turbulent velocity for $\gamma_{\text{eff}} = 1.09$ with different base grid sizes and Jeans Parameters (RM512–RM32). The degree of initial turbulence de-

creases from the left panel to the right in this figure.

In all models, the turbulence is amplified through gravitational contraction.

For $\mathcal{M}_0 = 0.0$, the initial turbulent velocities are totally numerical error, while the results for $\mathcal{M}_0 = 0.05$ are physical, as shown in Figure 13. Therefore, in Figure 14, we can see whether the results are physical or numerical by comparing the results of the other panels with the values in the rightmost panel. In the models RM32, RM64, and RM128, the results for $\mathcal{M}_0 = 0.01$ and $\mathcal{M}_0 = 0.005$ seem to be numerical because the turbulent velocity around the initial states of these models are comparable to that of $\mathcal{M}_0 = 0.0$. In the model RM256, it is a bit higher than that of $\mathcal{M}_0 = 0.0$. Hence, the results of this model may be affected by numerical disturbance, but not fully numerical. These results suggest the general trend that the resolution required to obtain the physical turbulent velocity increases as the initial Mach number decreases.

As for the $\mathcal{M}_0 = 0.05$ model, we observe the convergence of RM256 and RM512 in the leftmost panel including the saturated regime. Thus, the obtained results on the growth and the saturation of the turbulent velocity for $\mathcal{M}_0 = 0.05$ are real. Considering that the initial turbulent Mach number in a primordial star formation simulation is normally larger than $\mathcal{M}_0 = 0.05$ (e.g., Clark et al. 2011a; Riaz et al. 2018; Wollenberg et al. 2020), RM256 is enough to resolve the turbulence in those collapse simulations.

4.6. Effects of initial spectrum/solenoidal ratio

We finally test the effects of initial spectrum/solenoidal ratio of turbulence.

We have two sets of simulations here for $\mathcal{M}_0 = 0.05$ and $\gamma_{\text{eff}} = 1.09$.

1. Test for the different initial turbulent kinetic energy spectrum, such as $E(k) \propto k^{-1}$, k^{-2} , k^{-3} , and k^{-4} . The solenoidal ratio is fixed to the natural mixture (Test1).
2. Test for the different mode mixture for $E(k) \propto k^{-2}$, such as natural mixture, fully solenoidal mode, and fully compressive mode (Test2).

We plot the results of these test in Figure 15. This figure shows the evolution of the turbulent velocity as a function of mean density for Test1 (upper panel) and Test2 (lower panel).

In the upper panel, we can see that our analytic estimates are in good agreement with all of initial turbulent energy spectra. This means that the spectral indices do not change throughout the collapse at least on around the Jeans scale $\sim k_J$. This conservation of the spectral indices before the saturation is simply understood by the time scale argument. The time scale of cascade around the core scale (i.e. Jeans scale) is $\sim 1/(k_J v_{\text{turb}})$, which

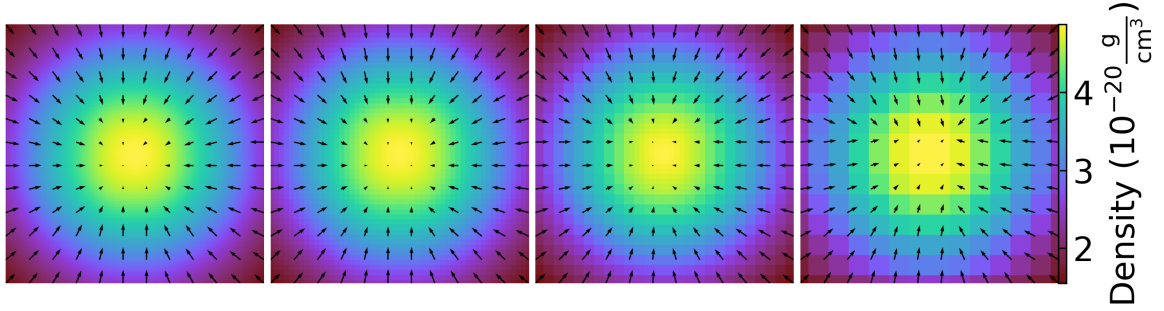


Figure 12. Slice plots of density in $z=0$ at $t = 100$ kyr corresponding to $\rho_{\text{mean}} \sim 1.8 \times 10^{-20} \text{ g cm}^{-3}$ in models RM256, RM128, RM64 and RM32. The color legend of density is shown on the right. The black arrows are velocity vector, and its length is in arbitrary unit. The box size is 1.0 pc.

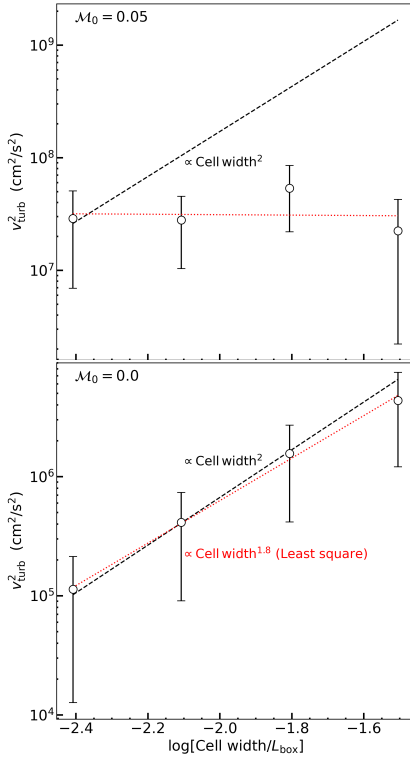


Figure 13. Scatter plot for the square of the disturbance vs. non dimensional cell width at $t = 100$ kyr corresponding to $\rho_{\text{mean}} \sim 1.8 \times 10^{-20} \text{ g cm}^{-3}$ in models RM32 - RM256 for $\mathcal{M}_0 = 0.05$ (upper panel) and for $\mathcal{M}_0 = 0.0$ (lower panel). A black dashed line corresponds to $\propto (\text{cell width})^2$. Red dotted lines are obtained by a least-square method.

is longer than the sound crossing time $\sim 1/(k_J c_s)$ as long as $v_{\text{turb}} < c_s$. This sound crossing time of the core should be comparable to the gravitational collapse time scale. As a result, the time scale of cascade is longer than the collapse time scale. Thus it is reasonable that the shape of the spectrum is conserved before the saturation (see also Figure 16 in details).

In the lower panel, the natural mixture model and the fully solenoidal model show almost identical results. The turbulent velocities in these two models are amplified

immediately after the collapse begins. In both cases the turbulent Mach numbers saturate at $\mathcal{M} \sim 2$, being independent on the initial mode mixture of turbulence.

In contrast, the fully compressive model shows a significant difference from above two models. The turbulent velocity in the fully compressive model decreases immediately after the collapse begins. This may be due to the oscillation of the small k -modes of compressive mode. The initial density fluctuation is set to be zero, while the (compressive) turbulent velocity is finite. This means that the amplitude of the initial turbulent velocity is at the local maximum of the oscillation, thereby it decreases initially. As the collapse proceeds, some of the energy of the compressive mode is converted to the solenoidal mode, which is already seen in Figure 9. Then the growth of the solenoidal mode is launched, eventually overtaking the compressive mode. Consequently the turbulent velocity increases with a growth rate similar to the other two models, i.e. the growth rate of the solenoidal mode finally dominates that of the compressive mode during the contraction even in the absence of the solenoidal mode at the onset of the collapse.

To reinforce the above argument for the upper panel in Figure 15, we also plot the evolution of the turbulent kinetic energy spectra (Figure 16) for the model of initial energy spectrum $E(k) \propto k^{-3}$ in Test1. The details of this figure are the same as Figure 9 except for the initial turbulent kinetic energy spectrum. In the upper panel, we can clearly see the conservation of spectral indices before the saturation ($\rho_{\text{mean}} < 10^{-8}$). In contrast, after the saturation, the spectral indices gradually increase (i.e. become shallower power-law distribution), starting from the high- k end. It is because smaller turbulent eddies at the high- k end firstly redistribute the energy in the k -space by the nonlinear effect, since the eddy time scales are shorter than those in low- k eddies.

Summarizing the results of these test, we find that the growth rate of the turbulent velocity sensitively depends on the initial power-law index of the turbulent kinetic energy spectrum. On the other hand, the growth rate is insensitive to the initial solenoidal ratio, following the

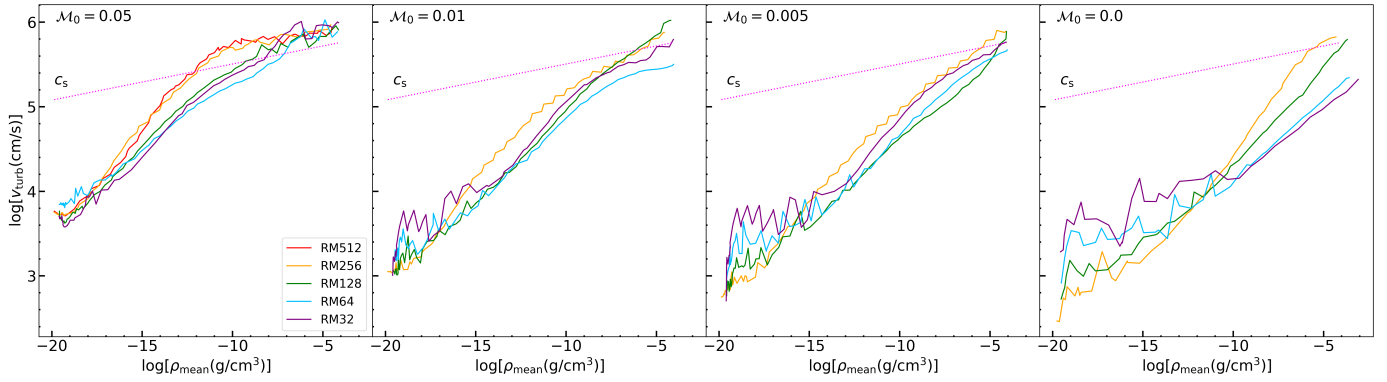


Figure 14. Evolution of the turbulent velocity as a function of mean density in models RM32–RM512 for $\gamma_{\text{eff}} = 1.09$. RM512 is prepared only for $\mathcal{M}_0 = 0.05$.

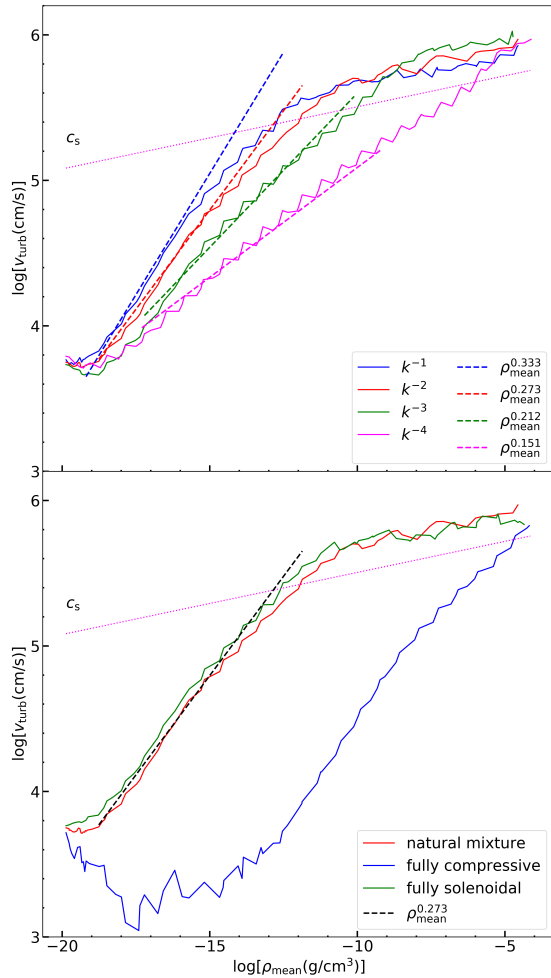


Figure 15. Evolution of the turbulent velocity as a function of mean density for Test1 (upper panel) and Test2 (lower panel). The solid curves with different colors denote the numerical results for different initial turbulence models. The magenta dotted line denotes the average sound speed in the Jeans volume. The dashed lines corresponding to each color in the upper panel and the black dashed line in the lower panel depict our analytic estimates (Equation 14).

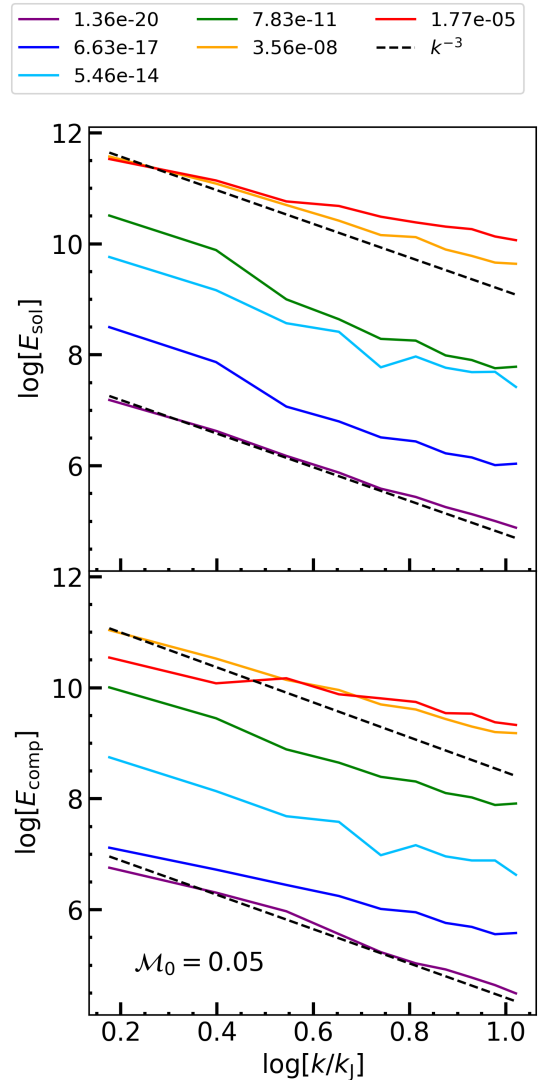


Figure 16. Evolution of the turbulent kinetic energy spectra of solenoidal modes (upper panel) and compressive modes (lower panel) for $\mathcal{M}_0 = 0.05$, respectively. The solid curves show the numerical results. The black dashed curves denotes $\propto k^{-3}$. The different colors indicate different values of ρ_{mean} .

growth rate of the solenoidal mode (Equation 14), although the launch of the growth is delayed for initially 100% compressive turbulence model. In all cases, the turbulent velocities grow, in agreement with the analytic estimate in Section 2.

5. DISCUSSION

We have set weak initial turbulence ($\mathcal{M}_0 \leq 0.1$) to understand the detailed evolution of turbulence. Cosmological simulations of other authors have shown that the gas inflow along the filaments of the halo already generates turbulence of $\mathcal{M}_0 \gtrsim 0.5$ in the low-density phase ($n_{\text{H}} \sim 10^3 \text{ cm}^{-3}$) before the run-away collapse begins (e.g., Wise & Abel 2007; Greif et al. 2008, 2011, 2012). These initial Mach numbers clearly exceed the threshold found in this paper (Equation 15), thereby the star forming dense core should reach the sonic point during the collapse. This is consistent with the previous numerical studies such as Greif et al. (2012). In addition, the saturation level of the turbulent velocities for $\gamma_{\text{eff}} = 1.09$ seems to be supersonic (Figure 4), that is also consistent with the results of Greif et al. (2012), in which the Mach number at the final phase is $\mathcal{M} \simeq 2$. Hence, our finding in this paper can well describe the numerical studies on first star formation so far.

We have used the initial conditions with an ideal Bonnor-Ebert sphere, which neglects the initial rotation and the asymmetry of clouds. Consequently, we have minimized the effects of the deformation and the shear motion triggered by the rotation. We also assume constant γ_{eff} , to simplify the entropy production/reduction processes, such as hydrodynamical shocks or radiative cooling. The presence of shock waves leads to the time variation of vorticity due to baroclinic term in the vorticity equation, which is neglected in this work. These assumptions could have some impact on the present results, which can be discussed by the comparison with a previous study. Greif et al. (2012) followed the gas collapse until protostellar cores form from cosmological initial conditions, considering various cooling processes and shock heating. Their simulations also result in the amplification of turbulence up to $\mathcal{M} \sim 2$, which is consistent with the results in this paper (Figure 4) although they only consider the cases starting from transonic turbulent velocities. This implies that the initial gas rotation and entropy variation have little impacts on the amplification of turbulence. Additionally, Turk et al. (2012) also followed the gas collapse from cosmological initial conditions as well as Greif et al. (2012) except for the presence of magnetic fields and the difference of a dynamic range. As a result, the density vs. vorticity squared relation in their calculations almost follows $\omega^2 \propto \rho^{4/3}$. This fact shows that the contribution of the baroclinic term in the vorticity equation is small in the collapse simulations.

In this paper, we have not investigated the turbulence in the mass accretion phase, which is important for the

dynamics of the disk fragmentation. The disks would form around hydrostatic cores (protostars) where radiative cooling is inefficient in the optically thick regime with densities $\rho_{\text{peak}} \gtrsim 10^{-5} \text{ g cm}^{-3}$ (Larson 1969; Penston 1969). Recent studies have shown that the initial turbulence can enhance disk fragmentation, and can affect the initial mass function (IMF) of the first generation of stars (e.g., Clark et al. 2011a; Riaz et al. 2018; Wollenberg et al. 2020). Because of the strong shear motion in the disk and the chaotic motions caused by the fragments, it is reasonable to expect that the turbulence is kept driven in the mass accretion phase.

Turbulent motion should be accompanied by magnetic fields, while it is not taken into account in the present paper. Presence of the magnetic fields is important for the protostellar evolution in general. It can introduce additional heating during the run-away collapse phase (Schleicher et al. 2009; Nakauchi et al. 2019, 2021), and magnetic breaking/outflow launching is activated in the mass accretion phase (Machida & Doi 2013). High-resolution numerical simulations show that, in the turbulent primordial gas with magnetic fields, the small-scale dynamo effect can amplify the seed magnetic fields to certain levels depending on the initial seed field strength and on the numerical resolution (Sur et al. 2010, 2012; Federrath et al. 2011; Turk et al. 2012). However, the numerical results do not converge even with the state-of-art highest-resolution simulations, because the eddy scale is too small compared to the Jeans scale to be resolved numerically. Therefore, the actual magnitude of the magnetic fields during the collapse phase in the first star-forming environment is still unknown. One possible direction to overcome this numerical difficulty is to introduce a sub-grid model based upon the analytic estimates (Schleicher et al. 2010; Schober et al. 2012; Xu & Lazarian 2016, 2020; McKee et al. 2020).

Finally, it is worthy to note that the present results are quite general and robust, thereby can be applied to not only the primordial case, but also to more general star formation/cloud collapse processes. Normally, cloud collapse simulations do not use large Jeans parameters, so that they fail to resolve the turbulent eddies, which could change the physical process in the core. Hence we have to keep in mind that run-away collapsing core tend to be turbulent, even if the initial seed velocity field is small.

6. SUMMARY

We study the amplification of turbulence in collapsing gas clouds by performing high-resolution numerical simulations until the gas peak density reaches $\rho_{\text{peak}} = 10^{-4} \text{ g cm}^{-3}$. We find that the turbulence can be amplified through the contraction of the gas cloud. We analytically estimate the scaling relation between the turbulent velocity/vorticity and density, and find that our simulation results are in good agreement with our

analytic estimates, although special care is necessary on the introduced error by grid discretization. We also find a critical initial Mach number at ρ_0 to achieve sonic/super sonic turbulence at a given density ρ_{sonic} . For $\rho_0 = 10^{-19} \text{ g cm}^{-3}$ and $\rho_{\text{sonic}} = 10^{-6} \text{ g cm}^{-3}$, we obtain $\mathcal{M}_{0,\text{cr}} \simeq 0.001$. As a result, highly turbulent dense cores are logically expected, since this initial Mach number is easily realized in cosmological simulations. To investigate the amplification mechanism in more detail, we follow the evolution of solenoidal and compressive velocity modes separately. The solenoidal mode is dominant from just after we start the simulations if we subtract the radial velocity from the total velocity. This indicates that the gravitational compression of clouds powers the amplification of solenoidal modes, and the total turbulent velocity increases. The solenoidal modes continue to grow until we terminate the simulations, and the turbulent velocity eventually reaches the supersonic velocity even with small initial Mach number $\mathcal{M}_0 = 0.05$. We finally test the effects of the initial spectrum/solenoidal ratio of the turbulence. It is found that the growth rate of the turbulence sensitively depends on the initial spectrum of the turbulence, which is also in agreement with our analytic estimate. On the other hand, the growth rate is same among the various initial

solenoidal ratio cases, simply because the growth rate is basically dominated by the solenoidal mode. These results indicate that the turbulence can play important roles in collapsing clouds in general cases.

ACKNOWLEDGMENTS

We are grateful to anonymous referee for careful reading of the manuscript and constructive comments. We thank K.Shima, K.Tomida, N.Yoshida, T.Matsumoto, and J.H.Wise for fruitful discussions and useful comments. We are thankful for the support by Ministry of Education, Science, Sports and Culture, Grants-in-Aid for Scientific Research No. 17H02869, 17H01101, and 17H06360. GC is supported by Overseas Research Fellowships of the Japan Society for the Promotion of Science (JSPS) for Young Scientists. A part of numerical calculations in this work was carried out on Yukawa-21 at the Yukawa Institute Computer Facility. Computations and analysis described in this work were performed using the publicly-available **Enzo** and **yt** codes, which is the product of a collaborative effort of many independent scientists from numerous institutions around the world.

REFERENCES

- Abel, T., Bryan, G. L., & Norman, M. L. 2002, *Science*, 295, 93, doi: [10.1126/science.295.5552.93](https://doi.org/10.1126/science.295.5552.93)
- Birnboim, Y., Federrath, C., & Krumholz, M. 2018, *MNRAS*, 473, 2144, doi: [10.1093/mnras/stx2426](https://doi.org/10.1093/mnras/stx2426)
- Bromm, V., Coppi, P. S., & Larson, R. B. 2002, *ApJ*, 564, 23, doi: [10.1086/323947](https://doi.org/10.1086/323947)
- Bryan, G. L., Norman, M. L., O’Shea, B. W., et al. 2014, *ApJS*, 211, 19, doi: [10.1088/0067-0049/211/2/19](https://doi.org/10.1088/0067-0049/211/2/19)
- Chiaki, G., & Yoshida, N. 2020, arXiv e-prints, arXiv:2008.06107. <https://arxiv.org/abs/2008.06107>
- Clark, P. C., Glover, S. C. O., Klessen, R. S., & Bromm, V. 2011a, *ApJ*, 727, 110, doi: [10.1088/0004-637X/727/2/110](https://doi.org/10.1088/0004-637X/727/2/110)
- Clark, P. C., Glover, S. C. O., Smith, R. J., et al. 2011b, *Science*, 331, 1040, doi: [10.1126/science.1198027](https://doi.org/10.1126/science.1198027)
- Dubinski, J., Narayan, R., & Phillips, T. G. 1995, *ApJ*, 448, 226, doi: [10.1086/175954](https://doi.org/10.1086/175954)
- Federrath, C., Sur, S., Schleicher, D. R. G., Banerjee, R., & Klessen, R. S. 2011, *ApJ*, 731, 62, doi: [10.1088/0004-637X/731/1/62](https://doi.org/10.1088/0004-637X/731/1/62)
- Fuller, T. M., & Couchman, H. M. P. 2000, *ApJ*, 544, 6, doi: [10.1086/317187](https://doi.org/10.1086/317187)
- Greif, T. H., Bromm, V., Clark, P. C., et al. 2012, *MNRAS*, 424, 399, doi: [10.1111/j.1365-2966.2012.21212.x](https://doi.org/10.1111/j.1365-2966.2012.21212.x)
- Greif, T. H., Johnson, J. L., Klessen, R. S., & Bromm, V. 2008, *MNRAS*, 387, 1021, doi: [10.1111/j.1365-2966.2008.13326.x](https://doi.org/10.1111/j.1365-2966.2008.13326.x)
- Greif, T. H., Springel, V., White, S. D. M., et al. 2011, *ApJ*, 737, 75, doi: [10.1088/0004-637X/737/2/75](https://doi.org/10.1088/0004-637X/737/2/75)
- Haiman, Z., Thoul, A. A., & Loeb, A. 1996, *ApJ*, 464, 523, doi: [10.1086/177343](https://doi.org/10.1086/177343)
- Hanawa, T., & Matsumoto, T. 2000, *PASJ*, 52, 241, doi: [10.1093/pasj/52.2.241](https://doi.org/10.1093/pasj/52.2.241)
- Hirano, S., & Bromm, V. 2017, *MNRAS*, 470, 898, doi: [10.1093/mnras/stx1220](https://doi.org/10.1093/mnras/stx1220)
- Inoue, S., & Yoshida, N. 2020, *MNRAS*, 491, L24, doi: [10.1093/mnrasl/slz160](https://doi.org/10.1093/mnrasl/slz160)
- James, R. A. 1977, *Journal of Computational Physics*, 25, 71, doi: [10.1016/0021-9991\(77\)90013-4](https://doi.org/10.1016/0021-9991(77)90013-4)
- Klessen, R. S., & Hennebelle, P. 2010, *A&A*, 520, A17, doi: [10.1051/0004-6361/200913780](https://doi.org/10.1051/0004-6361/200913780)
- Lai, D. 2000, *ApJ*, 540, 946, doi: [10.1086/309361](https://doi.org/10.1086/309361)
- Larson, R. B. 1969, *MNRAS*, 145, 271, doi: [10.1093/mnras/145.3.271](https://doi.org/10.1093/mnras/145.3.271)
- . 1981, *MNRAS*, 194, 809, doi: [10.1093/mnras/194.4.809](https://doi.org/10.1093/mnras/194.4.809)
- Mac Low, M.-M. 1999, *ApJ*, 524, 169, doi: [10.1086/307784](https://doi.org/10.1086/307784)
- Machida, M. N., & Doi, K. 2013, *MNRAS*, 435, 3283, doi: [10.1093/mnras/stt1524](https://doi.org/10.1093/mnras/stt1524)

- Mandal, A., Federrath, C., & Körtgen, B. 2020, MNRAS, 493, 3098, doi: [10.1093/mnras/staa468](https://doi.org/10.1093/mnras/staa468)
- Matsumoto, T., Dobashi, K., & Shimoikura, T. 2015, ApJ, 801, 77, doi: [10.1088/0004-637X/801/2/77](https://doi.org/10.1088/0004-637X/801/2/77)
- Matsumoto, T., & Hanawa, T. 2011, ApJ, 728, 47, doi: [10.1088/0004-637X/728/1/47](https://doi.org/10.1088/0004-637X/728/1/47)
- McKee, C. F., Stacy, A., & Li, P. S. 2020, MNRAS, 496, 5528, doi: [10.1093/mnras/staa1903](https://doi.org/10.1093/mnras/staa1903)
- Nakachi, D., Omukai, K., & Susa, H. 2019, MNRAS, 488, 1846, doi: [10.1093/mnras/stz1799](https://doi.org/10.1093/mnras/stz1799)
- . 2021, MNRAS, 502, 3394, doi: [10.1093/mnras/stab248](https://doi.org/10.1093/mnras/stab248)
- Nishi, R., & Susa, H. 1999, ApJL, 523, L103, doi: [10.1086/312277](https://doi.org/10.1086/312277)
- Omukai, K., & Nishi, R. 1998, ApJ, 508, 141, doi: [10.1086/306395](https://doi.org/10.1086/306395)
- Penston, M. V. 1969, MNRAS, 144, 425, doi: [10.1093/mnras/144.4.425](https://doi.org/10.1093/mnras/144.4.425)
- Prieto, J., Padoan, P., Jimenez, R., & Infante, L. 2011, ApJL, 731, L38, doi: [10.1088/2041-8205/731/2/L38](https://doi.org/10.1088/2041-8205/731/2/L38)
- Riaz, R., Bovino, S., Vanaverbeke, S., & Schleicher, D. R. G. 2018, MNRAS, 479, 667, doi: [10.1093/mnras/sty1635](https://doi.org/10.1093/mnras/sty1635)
- Robertson, B., & Goldreich, P. 2012, ApJL, 750, L31, doi: [10.1088/2041-8205/750/2/L31](https://doi.org/10.1088/2041-8205/750/2/L31)
- Schleicher, D. R. G., Banerjee, R., Sur, S., et al. 2010, A&A, 522, A115, doi: [10.1051/0004-6361/201015184](https://doi.org/10.1051/0004-6361/201015184)
- Schleicher, D. R. G., Galli, D., Glover, S. C. O., et al. 2009, ApJ, 703, 1096, doi: [10.1088/0004-637X/703/1/1096](https://doi.org/10.1088/0004-637X/703/1/1096)
- Schober, J., Schleicher, D., Federrath, C., et al. 2012, ApJ, 754, 99, doi: [10.1088/0004-637X/754/2/99](https://doi.org/10.1088/0004-637X/754/2/99)
- Sharda, P., Federrath, C., & Krumholz, M. R. 2020, MNRAS, 497, 336, doi: [10.1093/mnras/staa1926](https://doi.org/10.1093/mnras/staa1926)
- Stacy, A., Bromm, V., & Lee, A. T. 2016, MNRAS, 462, 1307, doi: [10.1093/mnras/stw1728](https://doi.org/10.1093/mnras/stw1728)
- Sur, S., Federrath, C., Schleicher, D. R. G., Banerjee, R., & Klessen, R. S. 2012, MNRAS, 423, 3148, doi: [10.1111/j.1365-2966.2012.21100.x](https://doi.org/10.1111/j.1365-2966.2012.21100.x)
- Sur, S., Schleicher, D. R. G., Banerjee, R., Federrath, C., & Klessen, R. S. 2010, ApJL, 721, L134, doi: [10.1088/2041-8205/721/2/L134](https://doi.org/10.1088/2041-8205/721/2/L134)
- Susa, H. 2013, ApJ, 773, 185, doi: [10.1088/0004-637X/773/2/185](https://doi.org/10.1088/0004-637X/773/2/185)
- . 2019, ApJ, 877, 99, doi: [10.3847/1538-4357/ab1b6f](https://doi.org/10.3847/1538-4357/ab1b6f)
- Susa, H., Hasegawa, K., & Tominaga, N. 2014, ApJ, 792, 32, doi: [10.1088/0004-637X/792/1/32](https://doi.org/10.1088/0004-637X/792/1/32)
- Suto, Y., & Silk, J. 1988, ApJ, 326, 527, doi: [10.1086/166114](https://doi.org/10.1086/166114)
- Tegmark, M., Silk, J., Rees, M. J., et al. 1997, ApJ, 474, 1, doi: [10.1086/303434](https://doi.org/10.1086/303434)
- Turk, M. J., Oishi, J. S., Abel, T., & Bryan, G. L. 2012, ApJ, 745, 154, doi: [10.1088/0004-637X/745/2/154](https://doi.org/10.1088/0004-637X/745/2/154)
- Turk, M. J., Smith, B. D., Oishi, J. S., et al. 2011, ApJS, 192, 9, doi: [10.1088/0067-0049/192/1/9](https://doi.org/10.1088/0067-0049/192/1/9)
- Wise, J. H., & Abel, T. 2007, ApJ, 671, 1559, doi: [10.1086/522876](https://doi.org/10.1086/522876)
- Wollenberg, K. M. J., Glover, S. C. O., Clark, P. C., & Klessen, R. S. 2020, MNRAS, doi: [10.1093/mnras/staa289](https://doi.org/10.1093/mnras/staa289)
- Xu, S., & Lazarian, A. 2016, ApJ, 833, 215, doi: [10.3847/1538-4357/833/2/215](https://doi.org/10.3847/1538-4357/833/2/215)
- . 2020, arXiv e-prints, arXiv:2007.11004. <https://arxiv.org/abs/2007.11004>
- Yoshida, N., Abel, T., Hernquist, L., & Sugiyama, N. 2003, ApJ, 592, 645, doi: [10.1086/375810](https://doi.org/10.1086/375810)
- Yoshida, N., Omukai, K., & Hernquist, L. 2008, Science, 321, 669, doi: [10.1126/science.1160259](https://doi.org/10.1126/science.1160259)
- Yoshida, N., Omukai, K., Hernquist, L., & Abel, T. 2006, ApJ, 652, 6, doi: [10.1086/507978](https://doi.org/10.1086/507978)